Research Article

Thanh Son Cam*, Tatyana Alekseevna Vishnievskaia, and Vadim Igorevich Popkov

Catalytic oxidation of CO over CuO/CeO_2 nanocomposites synthesized via solution combustion method: effect of fuels

https://doi.org/10.1515/rams-2020-0002
Received Sep 28, 2019; accepted Dec 11, 2019

Abstract: A series of CuO/CeO_2 catalysts were successfully synthesized via solution combustion method (SCS) using different fuels and tested for CO oxidation. The catalysts were characterized by energy-dispersive X-ray analysis (EDXA), X-ray diffraction (XRD), Fourier-transform infrared spectroscopy (FTIR), scanning electron microscope (SEM), N_2 adsorption-desorption isotherms and H_2 temperature-programmed reduction (H_2-TPR). It was found that the used fuels strongly affected the characterization and the low-temperature reduction behavior of CuO/CeO_2 catalysts. The CuO/CeO_2-urea catalyst exhibited higher catalytic activity toward CO oxidation (t_{50}=120°C, t_{100}=159°C) than the 5 other synthesized catalysts. In addition, the CuO/CeO_2-urea catalyst displayed high stability for CO oxidation during five cycles and water resistance. The enhanced catalytic CO oxidation of the synthesized samples can be attributed by a combination of factors, such as smaller crystallite size, higher specific surface area, larger amount of amorphous copper(II) oxide, more mesoporous and uniform spherical-like structure. These findings are worth considering in order to continue the study of the CuO/CeO_2 catalyst with low-temperature CO oxidation.

Keywords: CuO/CeO_2 nanocomposite, CO oxidation, solution combustion synthesis, fuels

1 Introduction

Many different catalysts have been prepared and tested for CO oxidation. For example, noble metal catalysts, such as gold nanoparticles [1], Pt-CeO_2/SiO_2 [2], Pt-group-metal [3], Ag/KIT-6 [4], Fe/Ag-15 [5, 6] have been demonstrated to be efficient on CO oxidation. It is known that gold nanoparticles are the best catalyst for CO oxidation at room temperature. However, due to limited availability, high cost, and sensitivity to sulfur poisoning of noble metals, more and more researchers are paying attention to new catalysts containing cheaper metals [7, 8]. In recent years, cerium dioxide (CeO_2) has been receiving quite a lot of attention because of its availability and high reactivity as a catalyst. The CeO_2 demonstrates high oxygen storage capacity, rich oxygen vacancies and the ability to easily switch between Ce^{3+} and Ce^{4+} [9]. In addition, its catalytic activity could be significantly increased if other metal ions, such as Cu^{2+}, were doped into the CeO_2 structure, which was due to the interaction of cerium with copper ions, causing a partial modification of the oxidation state through the formation of a redox pair (Ce^{4+}-Ce^{3+}/Cu^{+}-Cu^{2+}), this leads to the formation of stabilized Cu^{+}, which are active components involved in the adsorption of CO [10, 11]. The same situation is observed in other similar systems [12, 13]. A large number of CuO/CeO_2 were prepared by different methods and tested for the catalytic activity, for example, by co-precipitation [14] with the temperature (°C) for 50% CO conversion at t_{50}=116°C, by urea gelation/co-precipitation [15] with t_{50}=85°C, by solid-state impregnation [16] with t83=80°C, by co-precipitation, deposition-precipitation and impregnation [17] with CO total conversion at 85°C, by sol-gel [18] with t_{50}=117°C, by urea-nitrate combustion method [19] with t_{50}=95°C. Compared the catalytic CO oxidation of CuO/CeO_2 composites to alone oxide CuO [20, 21] with t_{50}=114°C or CeO_2 [22, 23] with t_{50}=240°C, 320°C and compared to other metal oxides, such Fe_2O_3 [24] with t_{50}=230°C, Mn_2O_3 [25, 26] with t_{50}=184°C, 213°C, the composites appear to be more activity.

***Corresponding Author: Thanh Son Cam:** Saint-Petersburg State Institute of Technology (Technical University), Moskovsky prospect 26, Saint-Petersburg, 190013, Russia; Email: camthanhson1108@gmail.com
Tatyana Alekseevna Vishnievskaia: Saint-Petersburg State Institute of Technology (Technical University), Moskovsky prospect 26, Saint-Petersburg, 190013, Russia
Vadim Igorevich Popkov: Ioffe Institute, Politekhnicheskaya Ulitsa 26, Saint-Petersburg, 194021, Russia

Table 1: Standard enthalpy of combustion of fuels (solid-state)

Fuel	ΔH_c^0, kJ/mol*	Fuel	ΔH_c^0, kJ/mol*
Urotropine ($C_6H_{12}N_4$)	−3936.20	α-D-Glucose ($C_6H_{12}O_6$)	−2541.00
Citric acid ($C_6H_8O_7$)	−3569.28	Ascorbic acid ($C_6H_8O_6$)	−2168.14
Glycine ($C_2H_5NO_2$)	−3456.46	Urea (CH_4N_2O)	−1088.14

* The data were calculated by the formula: $\Delta H_c^0(fuel) = \sum \Delta H_f^0(CO_2) + \sum \Delta H_f^0(H_2O) - \sum \Delta H_f^0(fuel)$.

From all the presented kinds of literature, we recognized that SCS possesses the preferential features that distinguish it from all other methods. Firstly, since SCS is a self-sustaining thermal process, so all we need is just to provide the initial heat for the reaction. In addition, the SCS method does not need complex equipment and the synthesis time is also fast. Secondly, in the SCS processes, the majority of the heat develops due to the burning of fuels, which can become a factor to control the desired characteristics of combustion products. Thirdly, the SCS processes generate a large number of gaseous byproducts. Such gases lead to a significant extension of the solid products, which make the powdered products porous and finely dispersed. Thus, due to the promising advantage of low cost and high activity, CuO/CeO_2 catalysts are expected to replace expensive noble metal catalysts in the future.

The basic principles of controlling the composition, size, morphology, and structure of SCS products are to regulate the chemical composition of the fuel, the oxidizer, the ratio between them and the solvents in the preparation step [27]. The work of Varma *et al.* [28] shows the diversity of the SCS-based method for nanosized materials and its potential commercialization pathways, a lot of SCS-related articles have been reported, but there is very little research on the effect of fuels on this method. Therefore, the purpose of this work is to synthesize the CuO/CeO_2 composites via the SCS method and to investigate the effect of fuels on the characteristics of synthesized products and how it affects the catalytic performance. Such findings can support the progress of CuO/CeO_2 catalysts for low-temperature oxidation of CO. The fuels selected in this work are most frequently used for the solution preparation, as mentioned in the review work of Varma *et al.* [28]. They are available, inexpensive, low decomposition temperature, and typically dissolved in a solvent with metal nitrate hydrates. The differences from the physical point of view between the used fuels were shown in Table 1, as can be seen, the standard enthalpy of combustion of fuels is different, resulting in their heat supply during combustion will also vary, therefore, the particles of the combustion products can be formed in different sizes. The differences from the chemical point of view between the types of fuel used are based on the difference in the molar mass, which determines the amount of gases that will be generated during the reaction, so the combustion products may be changed in different kinds of structure and morphology of the CuO/CeO_2 composites. In addition, various types of fuel form complexes with metal cations in solutions, as a result of which Cu particles will be dispersed differently on the surface of the CeO_2 lattice and these will definitely affect the catalytic performance of the CuO/CeO_2 catalysts.

2 Experimental

2.1 Catalyst preparation

The catalysts were synthesized according to the following redox reactions, the fuels used were urea (CH_4N_2O), citric acid ($C_6H_8O_7$), ascorbic acid ($C_6H_8O_6$), glucose ($C_6H_{12}O_6$), urotropine ($C_6H_{12}N_4$), and glycine ($C_2H_5NO_2$):

Urea:

$$8CH_4N_2O + 2Ce(NO_3)_3 + 2Cu(NO_3)_2 = 2(CuO/CeO_2) + 8CO_2\uparrow + 13N_2\uparrow + 16H_2O\uparrow \quad (1)$$

Citric acid:

$$8C_6H_8O_7 + 6Ce(NO_3)_3 + 6Cu(NO_3)_2 = 6(CuO/CeO_2) + 48CO_2\uparrow + 15N_2\uparrow + 32H_2O\uparrow \quad (2)$$

Ascorbic acid:

$$12C_6H_8O_6 + 10Ce(NO_3)_3 + 10Cu(NO_3)_2 = 10(CuO/CeO_2) + 72CO_2\uparrow + 25N_2\uparrow + 48H_2O\uparrow \quad (3)$$

Glucose:

$$2C_6H_{12}O_6 + 2Ce(NO_3)_3 + 2Cu(NO_3)_2 = 2(CuO/CeO_2) + 12CO_2\uparrow + 5N_2\uparrow + 12H_2O\uparrow \quad (4)$$

Urotropine:

$$4C_6H_{12}N_4 + 6Ce(NO_3)_3 + 6Cu(NO_3)_2 = 6(CuO/CeO_2) \quad (5)$$

$$+ 24CO_2 \uparrow + 23N_2 \uparrow + 24H_2O \uparrow$$

Glycine:

$$16C_2H_5NO_2 + 6Ce(NO_3)_3 + 6Cu(NO_3)_2 = 6(CuO/CeO_2) + 32CO_2 \uparrow + 23N_2 \uparrow + 40H_2O \uparrow \quad (6)$$

A detailed description of the synthesis of similar oxide systems is shown in the works [29, 30]. The steps of synthesis are as following (the number of reagents was taken in the stoichiometric ratio): first, the fuel was dissolved in the minimum volume of distilled water; next, cerium(III)-98.0% and copper(II)-99.0% nitrates were added to this solution; then, the solution was stirred until all components were completely dissolved; after that, the resulting solution was placed inside a stainless steel beaker, which was heated on a hot plate in air and maintained until complete evaporation of water from the solution; finally, the reaction mixture foamed, ignited, and burned to form a friable powder (Appendix 1, 2).

The combustion products were calcined at 500°C for 2 hours (heating rate 5°C/min) under an air atmosphere to remove the residual carbon and to obtain the stable catalysts, as were suggested in [31, 32]; then the final powders were analyzed using a complex of physicochemical methods. The obtained samples were named as CuO/CeO_2-urea, CuO/CeO_2-glycine, CuO/CeO_2-ascorbic, CuO/CeO_2-citric, CuO/CeO_2-glucose, and CuO/CeO_2-urotropine depending on the different used fuels.

2.2 Characterization methods

The microstructure of the samples, as well as their elemental composition, was analyzed by scanning electron microscopy on a TESCAN VEGA 3 SBH (Czech Republic) – scanning electron microscope, in the detection mode of secondary electrons ("relief mode").

X-ray diffraction analysis was performed on a RIGAKU SmartLab 3 Diffractometer with monochromatic CuK_α radiation (λ=0.15406 nm) in the range of Bragg angles (2θ) from 20° to 100° with a step scanning of 0.01°, a speed of 2°/min. Qualitative X-ray analysis was carried out using a powder X-ray diffraction database, quantitative X-ray analysis was performed using the Rietveld method. The average crystallite size (D) for spherical nanoparticles was calculated according to the Scherer equation:

$$D = \frac{0.9 \cdot \lambda}{\beta \cdot \cos(\theta)}, \quad (7)$$

where λ –X-ray wavelength, nm; β– full width at half maximum, in radians; θ– Bragg angle, in radians.

Fourier-transform infrared spectra were recorded using Shimadzu IRTracer-100 spectrometer with a resolution of 2 cm^{-1}, using 34 scans per spectrum in the range of 350–4000 cm^{-1}.

The specific surface area, total volume in pores, and pore size distribution of samples were determined using a Micrometrics ASAP 2020 with nitrogen as an adsorbate (N_2 adsorption-desorption isotherms at –196°C (77 K)).

H_2-TPR was performed on Chemosorb (SOLO, Russia) equipped with a thermal conductivity detector. The sample (80 mg) was pretreated in argon flow at 250°C for 30 min, then heated to 800°C at a ramp rate of 10°/min under a gas flow (60 ml/min) of H_2 (5 vol%) and Ar (95 vol%). CuO was used as an external reference for the calibration of hydrogen consumption. Frozen isopropanol with a temperature of about –90°C was used as a water trap.

2.3 Catalytic activity measurements

The catalytic oxidation of CO was carried out in a fixed-bed reactor system (the reactor tube consisted of stainless steel with fittings, the internal diameter of 0.9 cm and length of 47 cm) at the atmospheric pressure. In this work, preliminary preparation of the sample was taken by pressing the catalyst powder into a pellet with a pressure of 110 atm., then the pellet was flapped and put through a sieve to obtain small particles with a diameter of 0.8 mm. Measurements of CO oxidation were evaluated using 4 cm^3 of these small particles of catalyst (about 7 grams of each sample). The total gas-air flow rate was 1 liter per minute, which included 0.4% CO. The reaction temperature was controlled using a thermocouple placed on the outer wall of the reactor. The CO concentration in the reactor flow was analyzed using a "Tsvet-100, model 102" gas chromatograph (GC) equipped with a flame ionization detector attached to a column.

Contact time (t) of the gases with catalysts was determined by Eq. (8).

$$t = \frac{volume\ of\ catalyst}{flow\ rate\ of\ gas} = \frac{4 \cdot 60}{1000} = 0.24\ sec. \quad (8)$$

The CO conversion (x_{CO}) was calculated based on CO consumption (Eq. (9)). CO conversion from 0% to 100% took about 2 hours.

$$x_{CO}\,(\%) = \frac{n_{CO}^{in} - n_{CO}^{out}}{n_{CO}^{in}} \cdot 100, \quad (9)$$

where n_{CO}^{in} and n_{CO}^{out} are the corresponding peak area of the GC response at the inlet and outlet CO, respectively.

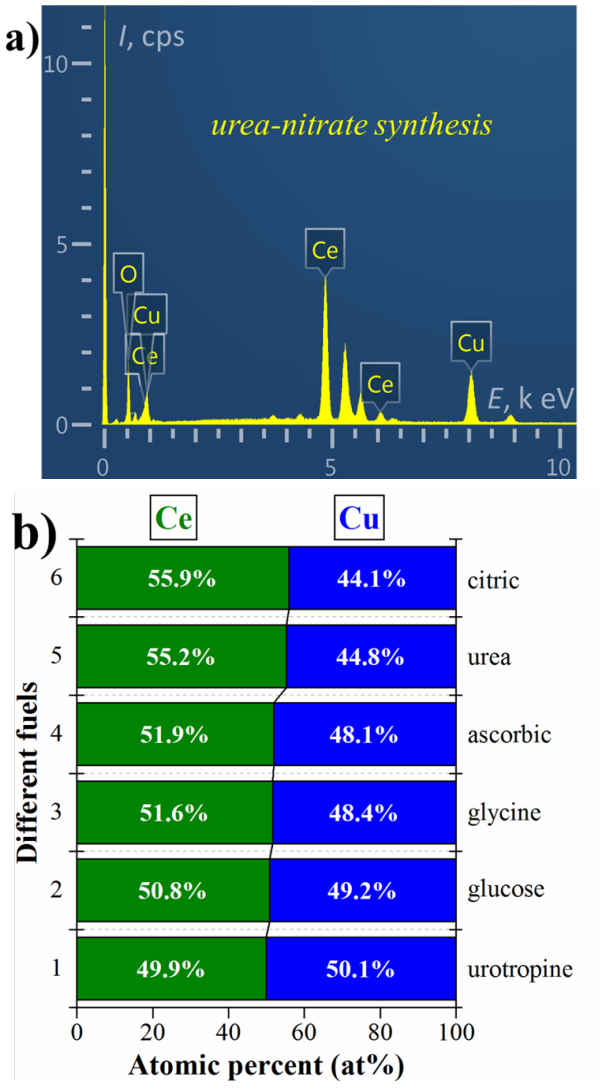

Figure 1: EDX spectra of CuO/CeO_2-urea sample (a); the ratio of Ce:Cu in the products obtained of CuO/CeO_2-urotropine, CuO/CeO_2-glucose, CuO/CeO_2-glycine, CuO/CeO_2-ascorbic, CuO/CeO_2-urea, CuO/CeO_2-citric, respectively, synthesized by the SCS method (b).

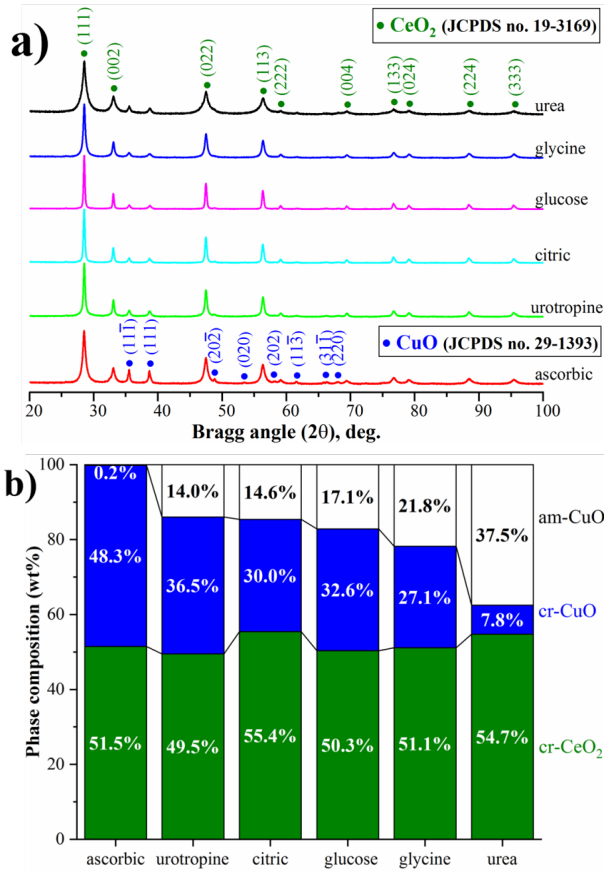

Figure 2: XRD patterns of the CuO/CeO_2-ascorbic, -urotropine, -citric, -glucose, -glycine, -urea samples synthesized by the SCS method (a); phase composition of 6 catalysts obtained (b).

3 Results and discussion

3.1 Characterization of catalysts

3.1.1 Energy-dispersive X-ray analysis

Figure 1a shows the purity of the CuO/CeO_2-urea sample, as evidenced by the presence of 3 elements Ce, Cu, and O in the EDX spectra, the 5 other samples also showed the same result. The synthesis of CuO/CeO_2 composites with an atomic ratio of Cu/Ce is 50/50 (or 1:1) according to the balanced chemical equation of each redox reaction presented in Eq. 1-6. The results obtained by EDXA method show the ratio of Cu/Ce is not actually of 50/50 (Figure 1b), but with deviation in the range of 0.1-5.9 at%, which can be explained by its local character (*i.e.* limited powder areas are analyzed).

3.1.2 Powder X-ray diffraction

The results from XRD patterns of the synthesized samples (Figure 2a) were compared with the Powder Diffraction Standards (JCPDS) of cerium and copper oxides, showing that all samples have obvious diffraction peaks that belong to crystalline CeO_2 (cr-CeO_2) with a cubic fluorite-type structure [14, 17, 33], but for the copper oxide phase, only a part of peaks is observed (cr-CuO, monoclinic structure) [34], some peaks are lower intensity and the others do not appear, so it can be said that a part of CuO species presents as an amorphous phase (am-CuO) on the catalyst surface. Therefore, we used the Rietveld method to determine the quantity of these phases. The calculated results

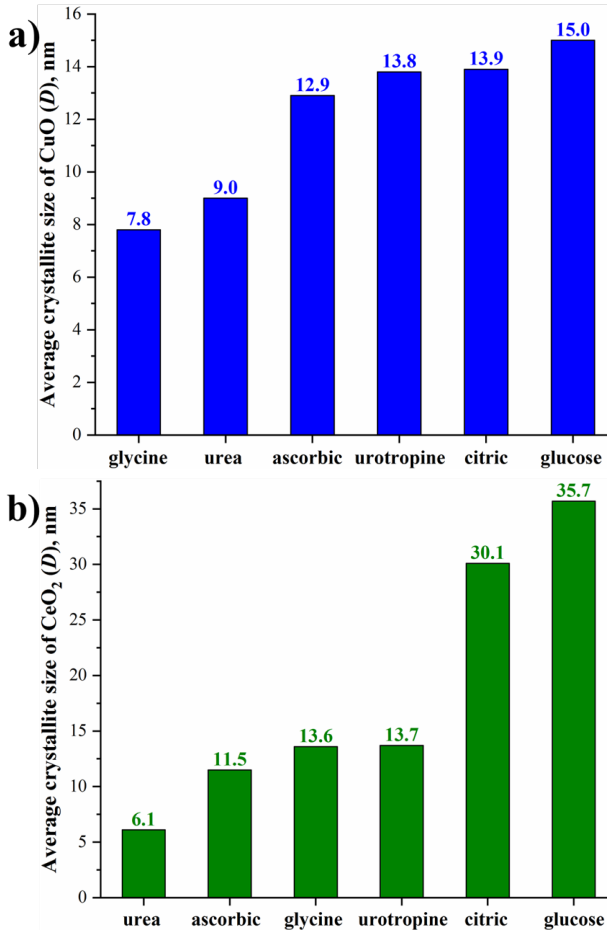

Figure 3: The average crystallite size of CuO (a) and CeO_2 (b).

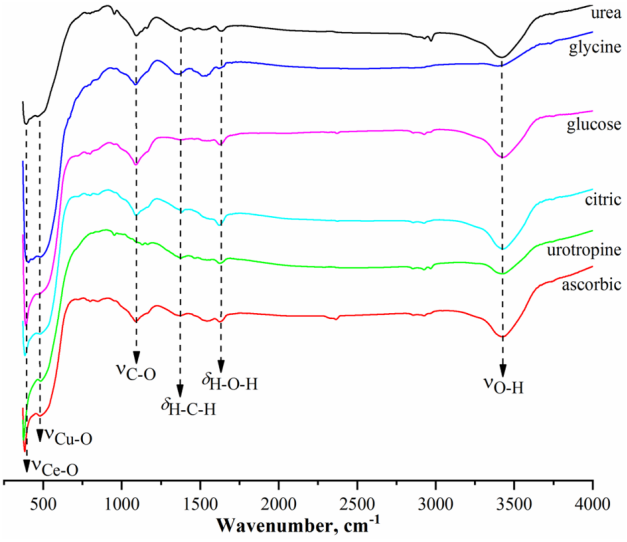

Figure 4: FTIR spectra of the synthesized CuO/CeO_2 composites.

are shown in Figure 2b. An amount of am-CuO phase in the catalyst changes when using different fuels, the most notable is the case of CuO/CeO_2-urea catalyst with the largest number of am-CuO. The change of the phase composition can be explained by the formation of complexes in different forms between fuels and metal cations and due to the different combustion temperatures in the synthesis process, *i.e.* different standard enthalpy of combustion ΔH_c^0 of fuels (Table 1).

The average crystallite size (D) was calculated by the Eq. (7) for each phase of the CuO/CeO_2 catalysts (Figure 3), the deviation due to the calculation is estimated at D±2 nm. Figure 3 indicates the different crystallite size of CuO and CeO_2 in the catalysts, remarkably pay attention to case of CuO/CeO_2-urea catalyst, the smallest size of CeO_2 is formed (6.1 nm), as a result of the presence of the largest amount of am-CuO, which leads to difficulties in association between CeO_2 itself particles. Because active sites involved in the adsorption of CO related to copper species on the catalyst surface, which means CuO/CeO_2-glycine catalyst with the smallest crystallite size of CuO (7.8 nm) promises to be a good candidate for high catalytic CO oxidation. In addition, the change in the crystallite size of the catalysts proved the different combustion temperatures in the reaction zone of each synthesis by using different types of fuel. Moreover, we have used the XRD results to report a crystallite size distribution of CuO and CeO_2, which is presented in Appendix 3.

3.1.3 FTIR spectral analysis

The functional groups on the surface of the prepared catalysts are shown on the FTIR spectra (Figure 4). The wavenumber of peaks in the region of 375-405 cm^{-1} can be attributed to vibrations of $\nu_{(Ce-O)}$ bonds [35], and $\nu_{(Cu-O)}$ bonds in the region of 465-485 cm^{-1} [36]. Furthermore, adsorbed $\delta_{(H-O-H)}$ water bonds (1618-1637 cm^{-1}) and $\nu_{(O-H)}$ hydrogen bonds (3421-3434 cm^{-1}) are also presented on the catalyst surface, which indicates the amount of moisture absorbed by the samples in the air [37]. Also, there are vibrations of $\nu_{(C-H)}$ (2854-2971 cm^{-1}), $\delta_{(H-C-H)}$ (1356-1386 cm^{-1}), and $\nu_{(C-O)}$ (1085-1095 cm^{-1}) bonds, which indicate traces of ethanol used for cleaning experimental instruments and equipment.

3.1.4 Scanning electron microscopy

Figure 5 shows SEM micrographs with a resolution of 2μm for all catalysts. On the basis of SEM data, it is shown that the type of fuel used displays a strong effect on the morphology of the combustion products: spherical-like struc-

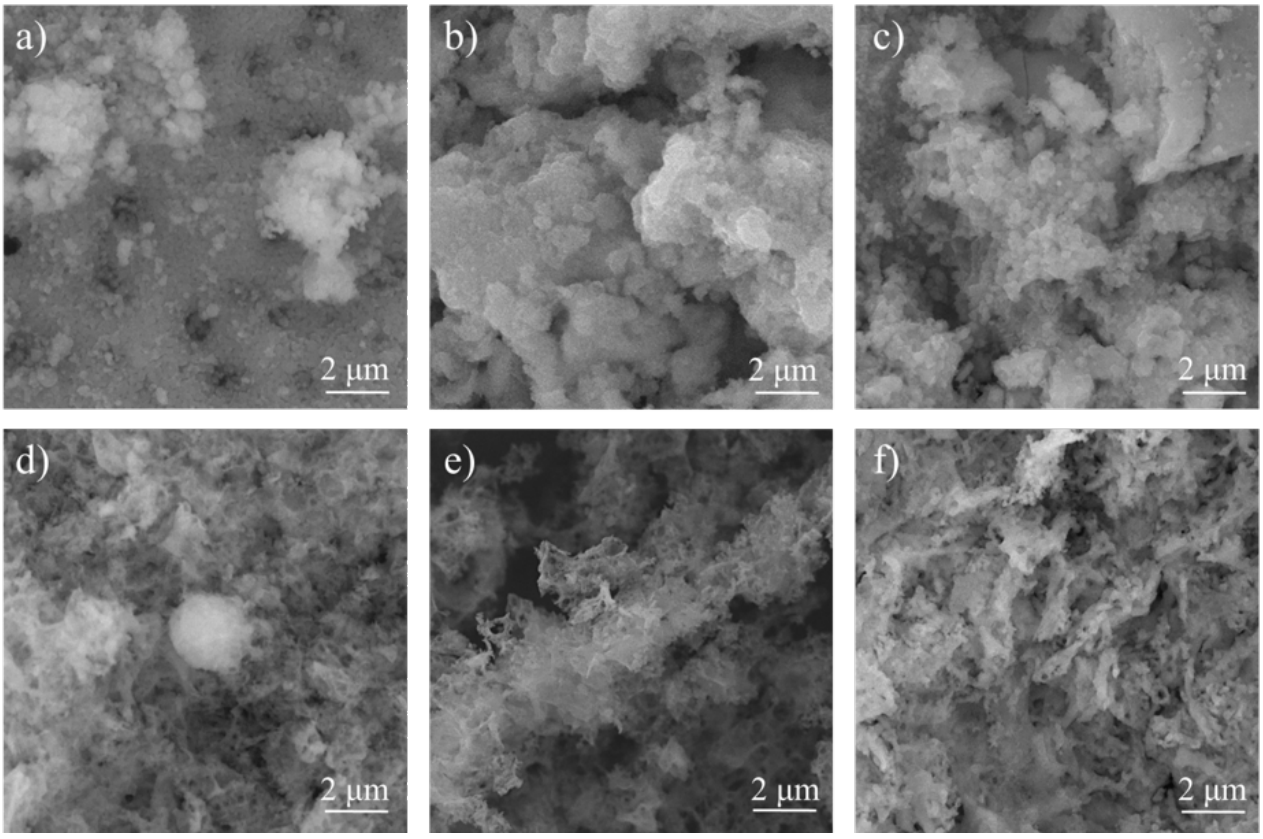

Figure 5: SEM micrographs of CeO_2/CuO nanocomposites with the following fuels used: a) urea; b) glycine; c) urotropine; d) ascorbic acid; e) citric acid; f) glucose.

tures [11, 37, 38] were formed for CuO/CeO_2-urea, -glycine, -urotropine catalysts; sponge-like morphology is observed when using ascorbic acid, citric acid, and glucose as the fuel. A more uniform morphology was obtained by using urea. All types are formed by isotropic nanoparticles agglomerated in micron-sized structures. The amount of gases generated during the reaction of each 6 syntheses is different as observed by us during the experiment, which may result in the formation of differently porous, foamy products.

3.1.5 Low-temperature nitrogen adsorption-desorption

The porous structure of the CuO/CeO_2 catalysts was evaluated by the N_2 adsorption-desorption isotherms at –196°C (Figure 6), Figure 6a reveals that all catalysts display type IV curves (according to the IUPAC classification of adsorption isotherms), which are characteristic of adsorbents that are mesoporous materials [7, 39]. Moreover, pore size distributions are established by DFT (density functional theory) calculated from the adsorption branch of the isotherms (Figure 6b) and Barrett-Joyner-Halenda (BJH) method calculated from the desorption branch of the isotherms (Figure 6c). Figure 6b shows that the pore diameter of the samples focuses in the mesoporous range of 23 and 37 nm, whereas the mode diameter obtained by applying the BJH theory is smaller than compared to the DFT result (in the range of 1-5 nm). Figure 6d shows the specific surface area S_{BET} (Brunauer-Emmett-Teller method) and total volume in pores V_{DFT} of the catalysts. The S_{BET} values increase in the series catalysts: CuO/CeO_2-glucose < CuO/CeO_2-urotropine < CuO/CeO_2-citric < CuO/CeO_2-glycine < CuO/CeO_2-ascorbic < CuO/CeO_2-urea. The largest specific surface area (21.7 m^2/g) belongs to the case of CuO/CeO_2-urea sample due to the smaller crystallite size of CeO_2, in contrast, compared to the case of CuO/CeO_2-glucose catalyst. The more porous on the surface catalyst is discovered by the V_{DFT} values: CuO/CeO_2-ascorbic > CuO/CeO_2-urea > CuO/CeO_2-glycine.

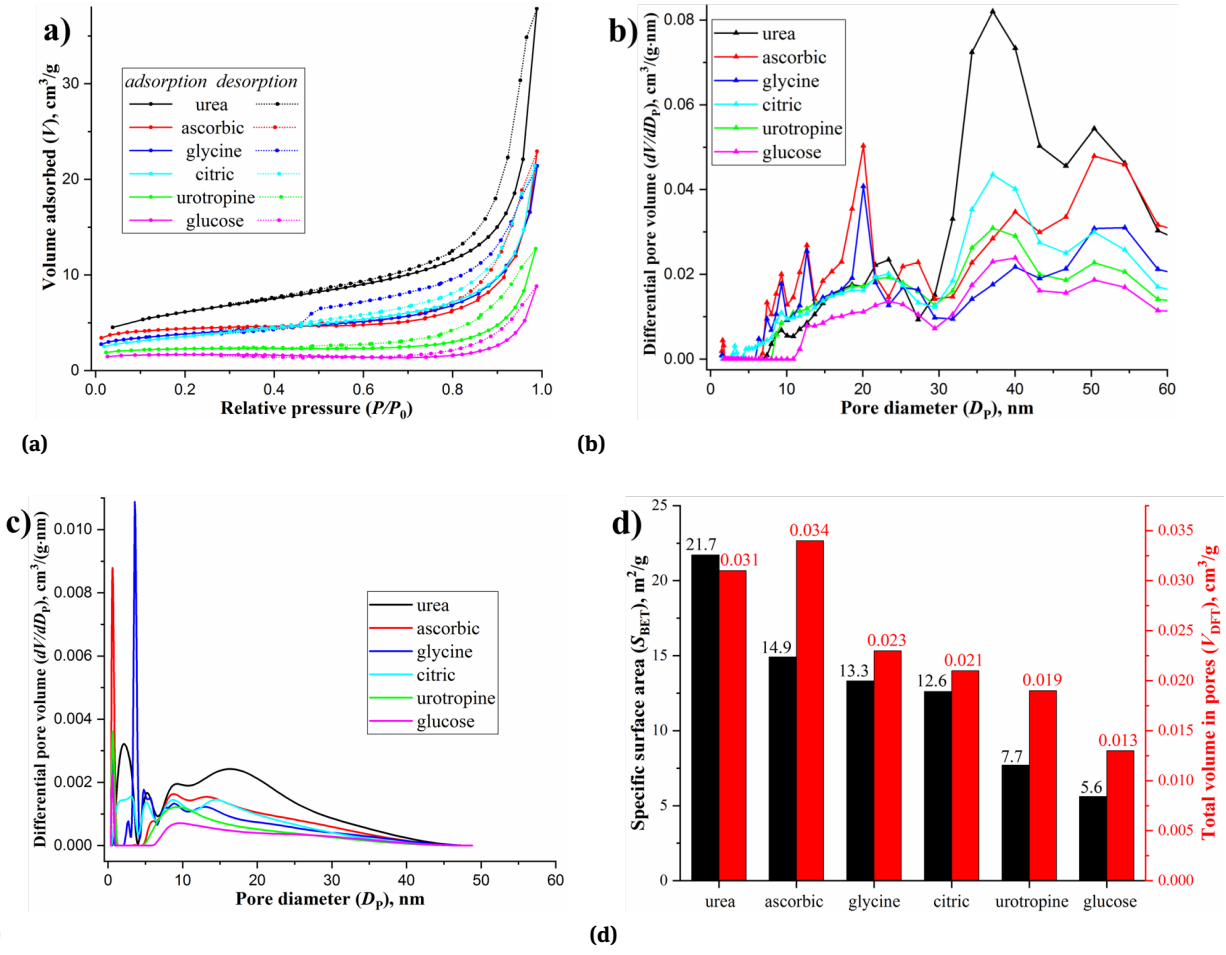

Figure 6: Results of N_2 adsorption-desorption isotherms (a); DFT pore size distribution curves (b); BJH pore size distribution curves (c); specific surface area and total volumes in pores of the synthesized samples.

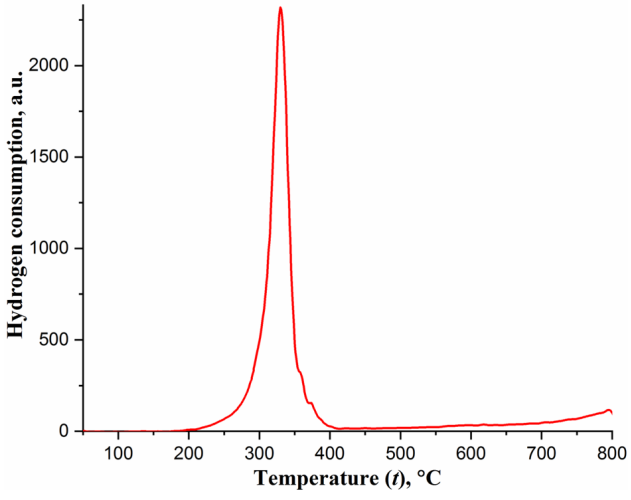

Figure 7: H_2-TPR profile of CuO/CeO_2-urea sample.

3.1.6 H_2-temperature-programmed reduction

Because of the CuO/CeO_2-urea catalyst possesses the most perspective characteristics for catalysis, therefore its reducibility is further studied by H_2-TPR profile. The TPR profile shows a single reduction peak at 330°C. This finding indicates a concurrent reduction of the copper oxide species and surface CeO_2 takes place owing to the synergic interaction between CuO and CeO_2. The same situation is found from work [40]. The reduction peak for CeO_2 does not appear, because CeO_2 is favorable to the formation of strongly, easily reducible surface copper species and is overlapped with that of CuO [41].

3.2 Catalytic performance

The catalytic activity of all catalysts is shown in Figure 8a. Among these catalysts, CuO/CeO_2-urotropine exhibits the

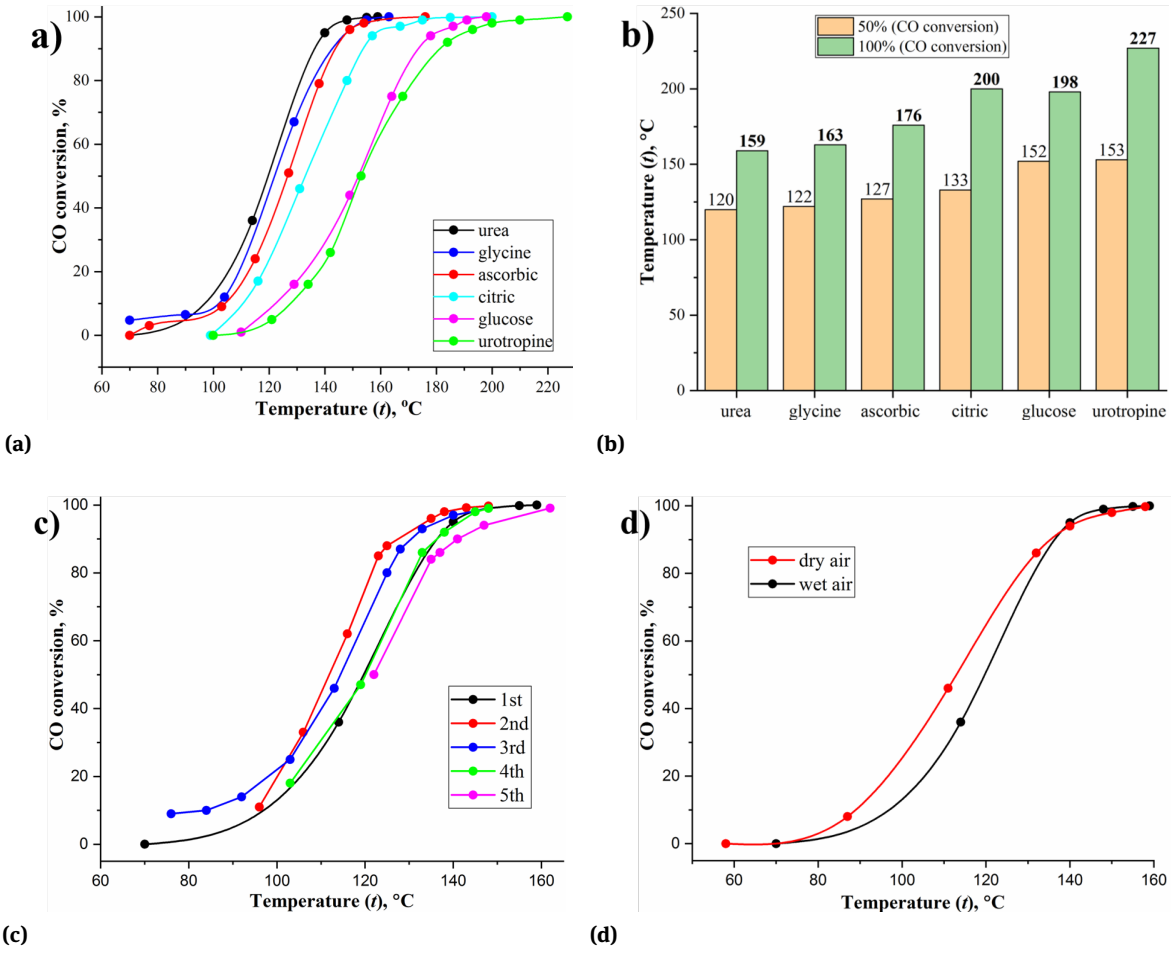

Figure 8: Results of measuring catalytic CO oxidation: a) temperature dependence of CO conversion over different catalysts; b) temperature of CO conversion at 50% and 100%; c) catalytic performance of the CuO/CeO_2-urea catalyst reused for five times; d) effect of water vapor on CO oxidation over CuO/CeO_2-urea catalyst.

lowest activity with temperature for 50% CO conversion (t_{50}) is 153°C, while the CuO/CeO_2-urea catalyst is the most active with t_{50} is 120°C (Figure 8b). It can be observed that the catalytic activity of the samples is highly related to their S_{BET}, which means that with an increase in the specific surface area, the catalytic activity also increases, but it is not a deciding factor, according to the characteristics of catalysts discussed above, the high catalytic CO oxidation of both CuO/CeO_2-urea and CuO/CeO_2-glycine catalysts can be explained by the large number of amorphous CuO phase on surface catalyst, the more porous property, the smaller crystallite size of CuO and CeO_2, the spherical-like structure and the more uniform morphology. The CuO/CeO_2-glucose catalyst possesses the largest crystallite size of both CuO and CeO_2, which explains its low activity for CO oxidation.

Compared with the same system of CuO/CeO_2 composites derived from in-situ synthesis, mechanical mixing and impregnation methods [42, 43] and through the direct decomposition [41] with the t_{50}=71, 102°C, our CuO/CeO_2-urea catalyst exhibit high comparative catalytic performance toward CO oxidation, but in the base of present work, if we have already determined the optimal fuel, we can further synthesize the CuO/CeO_2 catalysts by changing the ratio of fuel/oxidizer or ratio of CuO to CeO_2 in order to obtain the higher specific surface area and the more quantity of surface-active oxygen species of the catalysts, which are the determinants for low-temperature of CO oxidation.

The best catalyst obtained (CuO/CeO_2-urea) from the synthesized samples are further investigated its circularity and effect of water vapor. Figure 8c shows that after reused five times, the catalyst still maintains a high catalytic per-

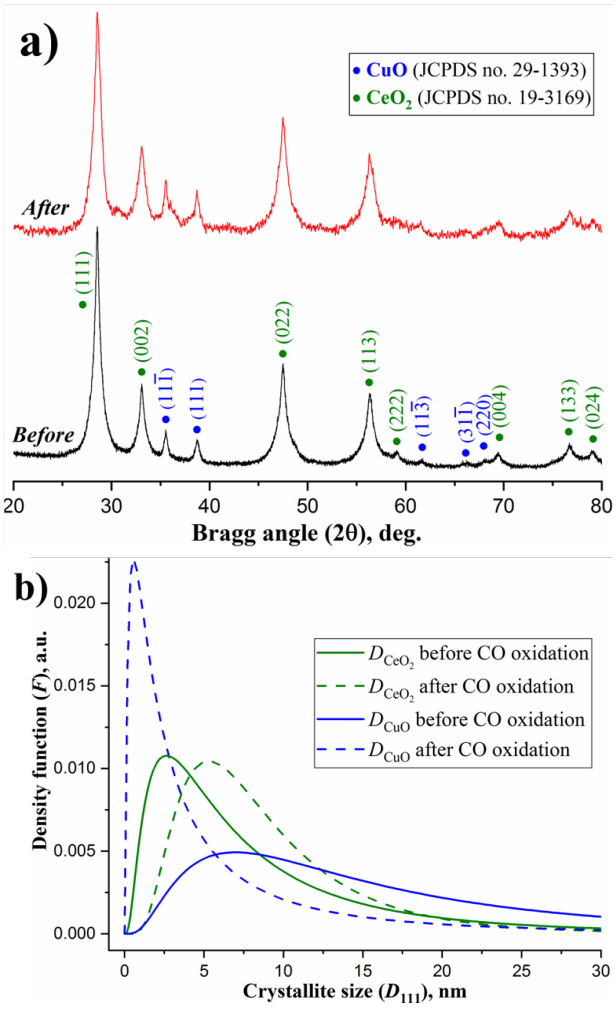

Figure 9: XRD pattern of CuO/CeO_2-urea catalyst derived from the SCS method before and after CO oxidation (a); crystallite size distribution of CuO and CeO_2 nanoparticles obtained before and after CO oxidation (b).

Table 2: Characterization of CuO/CeO_2-urea catalyst after carrying out the oxidation of CO with five cycles

CuO/CeO_2-urea catalyst	S_{BET}, m^2/g [a]	V_{DFT}, cm^3/g [b]	D_P, nm [c]
Before CO oxidation	21.7	0.031	23 (BJH) 37 (DFT)
After CO oxidation	12.2	0.016	23 (BJH) 37 (DFT)

[a] Brunauer–Emmett–Teller (BET) specific surface are;

[b] Total volume in pores measured at $P/P_0 = 0.99$;

[c] The pore diameter calculated from the desorption branch of the isotherm using the Barrett-Joyner-Halenda (BJH) or Density Functional Theory (DFT) method.

formance. Moreover, CuO/CeO_2-urea has been undergone an experiment in the presence of water vapor with relative humidity (RH) of 70% and the absence of water vapor with RH=7%. The result (Figure 8d) shows that, in the presence of water vapor, the catalyst exhibits a little inactive effect on CO oxidation as concluded of works [22, 23, 25, 26], but after temperatures exceed 130°C, it works normally again.

After carrying out the oxidation of CO with five cycles, the characterizations of the CuO/CeO_2-urea catalyst are further studied by XRD and N_2 adsorption-desorption isotherms. The results are presented in Figure 9 and Table 2. Figure 9 reveals that after CO oxidation, the phase composition of the composite is still kept the same, the crystallite size of CeO_2 is almost no change, but the size of CuO becomes smaller after CO oxidation. The S_{BET} and V_{DFT} values decrease (Table 2) may be due to pressing the catalyst powder into a pellet during sample preparation for CO oxidation.

4 Conclusions

The CuO/CeO_2 samples were obtained by the SCS method using different types of fuel. The fuels greatly affect the characteristics of the synthesized catalysts and their catalytic performance. The optimal fuel was determined for the combustion method for synthesizing the CuO/CeO_2 catalyst – urea, CuO/CeO_2-urea catalyst possesses the preferential properties for CO oxidation, such as a small crystallite size of both CuO, CeO_2, a high specific surface area, a large amount of amorphous CuO species, large mesoporous and uniform spherical-like structure. It is advisable to continue studying the optimal conditions for the synthesis of CuO/CeO_2 catalysts based on the SCS method to obtain a catalyst with low-temperature CO oxidation, which can be implemented in practical applications in the future.

Acknowledgement: This research did not receive any specific grant from funding agencies in the public, commercial, or not-for-profit sectors.

References

[1] Sun, K. Theoretical investigations on CO oxidation reaction catalyzed by gold nanoparticles. *Chinese Journal of Catalysis*, Vol. 37, No. 10, 2016, pp. 1608–1618.

[2] Punde, S. S., and B. J. Tatarchuk. Pt-CeO_2/SiO_2 catalyst for CO oxidation in humid air at ambient temperature. *Chinese Journal of Catalysis*, Vol. 38, No. 3, 2017, pp. 475–488.

[3] Lin, J., X. Wang, and T. Zhang. Recent progress in CO oxidation over Pt-group-metal catalysts at low temperatures. *Chinese Journal of Catalysis*, Vol. 37, No. 11, 2016, pp. 1805–1813.

[4] Yang, Y., F. Hou, H. Li, N. Liu, Y. Wang, and X. Zhang. Facile synthesis of Ag/KIT-6 catalyst via a simple one pot method and application in the CO oxidation. *Journal of Porous Materials*, Vol. 24, No. 6, 2017, pp. 1661–1665.

[5] Zhang, X., Y. Yang, L. Song, Y. Wang, C. He, Z. Wang, and L. Cui. High and stable catalytic activity of Ag/Fe 2 O 3 catalysts derived from MOFs for CO oxidation. *Mol. Catal.*, Vol. 447, 2018, pp. 80–89.

[6] Zhang, X., Y. Yang, X. Lv, Y. Wang, and L. Cui. Effects of preparation method on the structure and catalytic activity of Ag-Fe_2O_3 Catalysts Derived from MOFs. *Catalysts*, Vol. 7, No. 12, 2017, id. 382.

[7] Harrison, P. G., I. K. Ball, W. Azelee, W. Daniell, and D. Goldfarb. Nature and surface redox properties of copper(II)-promoted cerium(IV) oxide CO-oxidation catalysts. *Chemistry of Materials*, Vol. 12, No. 12, 2000, pp. 3715–3725.

[8] Sedmak, G., S. Hočevar, and J. Levec. Transient kinetic model of CO oxidation over a nanostructured Cu0.1Ce0.9O2-y catalyst. *Journal of Catalysis*, Vol. 222, No. 1, 2004, pp. 87–99.

[9] Lermontov, S. A., A. N. Malkova, L. L. Yurkova, A. Y. Baranchikov, and V. K. Ivanov. Nanosyst. Physics. *Chem. Math.*, Vol. 4, 2013, pp. 690–695.

[10] Shang, H., X. Zhang, J. Xu, and Y. Han. Effects of preparation methods on the activity of CuO/CeO_2 catalysts for CO oxidation. *Front. Chem. Sci. Eng.*, Vol. 11, No. 4, 2017, pp. 603–612.

[11] Cecilia, J., A. Arango-Díaz, J. Marrero-Jerez, P. Núñez, E. Moretti, L. Storaro, and E. Rodríguez-Castellón. Catalytic Behaviour of CuO-CeO_2 Systems Prepared by Different Synthetic Methodologies in the CO-PROX Reaction under CO2-H2O Feed Stream. *Catalysts*, Vol. 7, No. 5, 2017, p. 160.

[12] Zvereva, V. V., and V. I. Popkov. Synthesis of $CeO_2Fe_2O_3$ nanocomposites via controllable oxidation of CeFeO3 nanocrystals. *Ceramics International*, Vol. 45, No. 9, 2019, pp. 12516–12520.

[13] Popkov, V. I., V. P. Tolstoy, S. O. Omarov, and V. N. Nevedomskiy. Enhancement of acidic-basic properties of silica by modification with CeO_2-Fe_2O_3 nanoparticles via successive ionic layer deposition. *Applied Surface Science*, Vol. 473, 2019, pp. 313–317.

[14] Jung, C. R., J. Han, S. W. Nam, T. H. Lim, S. A. Hong, and H. I. Lee. Selective oxidation of CO over CuO-CeO_2 catalyst: Effect of calcination temperature. *Catalysis Today*, Vol. 93–95, 2004, pp. 183–190.

[15] Liu, Y., Q. Fu, and M. F. Stephanopoulos. Preferential oxidation of CO in H2 over CuO-CeO_2 catalysts. *Catalysis Today*, Vol. 93–95, 2004, pp. 241–246.

[16] Sun, J., L. Zhang, C. Ge, C. Tang, and L. Dong. Comparative study on the catalytic CO oxidation properties of CuO/CeO_2 catalysts prepared by solid state and wet impregnation. *Chinese Journal of Catalysis*, Vol. 35, No. 8, 2014, pp. 1347–1358.

[17] Tang, X., B. Zhang, Y. Li, Y. Xu, Q. Xin, and W. Shen. Carbon monoxide oxidation over CuO/CeO_2 catalysts. *Catalysis Today*, Vol. 93–95, 2004, pp. 191–198.

[18] Avgouropoulos, G., T. Ioannides, C. Papadopoulou, J. Batista, S. Hocevar, and H. K. Matralis. A comparative study of Pt/γ-Al2O3, Au/α-Fe_2O_3 and CuO–CeO_2 catalysts for the selective oxidation of carbon monoxide in excess hydrogen. *Catalysis Today*, Vol. 75, No. 1-4, 2002, pp. 157–167.

[19] Avgouropoulos, G., and T. Ioannides. Selective CO oxidation over CuO-CeO_2 catalysts prepared via the urea–nitrate combustion method. *Applied Catalysis A, General*, Vol. 244, No. 1, 2003, pp. 155–167.

[20] Yang, Y., H. Dong, Y. Wang, Y. Wang, N. Liu, D. Wang, and X. Zhang. A facile synthesis for porous CuO/Cu2O composites derived from MOFs and their superior catalytic performance for CO oxidation. *Inorganic Chemistry Communications*, Vol. 86, 2017, pp. 74–77.

[21] Yang, Y., H. Dong, Y. Wang, C. He, Y. Wang, and X. Zhang. Synthesis of octahedral like Cu-BTC derivatives derived from MOF calcined under different atmosphere for application in CO oxidation. *Journal of Solid State Chemistry*, Vol. 258, 2018, pp. 582–587.

[22] Zhang, X., F. Hou, H. Li, Y. Yang, Y. Wang, N. Liu, and Y. Yang. A strawsheave-like metal organic framework Ce-BTC derivative containing high specific surface area for improving the catalytic activity of CO oxidation reaction. *Microporous and Mesoporous Materials*, Vol. 259, 2018, pp. 211–219.

[23] Zhang, X., F. Hou, Y. Yang, Y. Wang, N. Liu, D. Chen, and Y. Yang. A facile synthesis for cauliflower like CeO_2 catalysts from Ce-BTC precursor and their catalytic performance for CO oxidation. *Applied Surface Science*, Vol. 423, 2017, pp. 771–779.

[24] Cui, L., D. Zhao, Y. Yang, Y. Wang, and X. Zhang. Synthesis of highly efficient α-Fe 2 O 3 catalysts for CO oxidation derived from MIL-100(Fe). *Journal of Solid State Chemistry*, Vol. 247, 2017, pp. 168–172.

[25] Zhang, X., H. Li, F. Hou, Y. Yang, H. Dong, N. Liu, Y. Wang, and L. Cui. Synthesis of highly efficient Mn 2 O 3 catalysts for CO oxidation derived from Mn-MIL-100. *Applied Surface Science*, Vol. 411, 2017, pp. 27–33.

[26] Zhang, X., H. Li, X. Lv, J. Xu, Y. Wang, C. He, et al. Facile synthesis of highly efficient amorphous Mn-MIL-100 catalysts: formation mechanism and structure changes during Application in CO Oxidation. *Chemistry (Weinheim an der Bergstrasse, Germany)*, Vol. 24, No. 35, 2018, pp. 8822–8832.

[27] Kondrashkova, I. S., K. D. Martinson, N. V. Zakharova, and V. I. Popkov. Synthesis of Nanocrystalline HoFeO3 Photocatalyst via Heat Treatment of Products of Glycine-Nitrate Combustion. *Russian Journal of General Chemistry*, Vol. 88, No. 12, 2018, pp. 2465–2471.

[28] Varma, A., A. S. Mukasyan, A. S. Rogachev, and K. V. Manukyan. Solution combustion synthesis of nanoscale materials. *Chemical Reviews*, Vol. 116, No. 23, pp. 14493–14586.

[29] Zaboeva, E. A., S. G. Izotova, and V. I. Popkov. Glycine-nitrate combustion synthesis of CeFeO3-based nanocrystalline powders. *Russian Journal of Applied Chemistry*, Vol. 89, No. 8, 2016, pp. 1228–1236.

[30] Komlev, A. A., and V. V. Gusarov. Glycine-nitrate combustion synthesis of nonstoichiometric Mg-Fe spinel nanopowders. *Inorganic Materials*, Vol. 50, No. 12, 2014, pp. 1247–1251.

[31] Popkov, V. I., V. P. Tolstoy, and V. N. Nevedomskiy. Peroxide route to the synthesis of ultrafine CeO_2-Fe_2O_3 nanocomposite via successive ionic layer deposition. *Heliyon*, Vol. 5, No. 3, 2019, id. e01443.

[32] Kotlovanova, N. E., A. N.Matveeva, S. O.Omarov, V. V. Sokolov, D. N. Akbaeva, and V. I. Popkov. Formation and acid-base surface properties of highly dispersed η-Al_2O_3 nanopowders. *Inorganic Materials*, Vol. 54, No. 4, 2018, pp. 392–400.

[33] Gómez-Cortés, A., Y. Márquez, J. Arenas-Alatorre, and G. Díaz. Selective CO oxidation in excess of H2 over high-surface area CuO/CeO_2 catalysts. *Catalysis Today*, Vol. 133–135, 2008, pp.

743–749.

[34] Wang, S., Q. Li, F. Chen, J. Ke, and R. Chen. HEPES-mediated controllable synthesis of hierarchical CuO nanostructures and their analogous photo-Fenton and antibacterial performance. *Advanced Powder Technology*, Vol. 28, No. 5, 2017, pp. 1332–1339.

[35] Chae, B. W., T. Amna, M. S. Hassan, S. S. Al-Deyab, and M. S. Khil. CeO_2-Cu2O composite nanofibers: Synthesis, characterization photocatalytic and electrochemical application. *Advanced Powder Technology*, Vol. 28, No. 1, 2017, pp. 230–235.

[36] Jeyarani, W. J., T. Tenkyong, N. Bachan, D. A. Kumar, and J. M. Shyla. An investigation on the tuning effect of glucose-capping on the size and bandgap of CuO nanoparticles. *Advanced Powder Technology*, Vol. 27, No. 2, 2016, pp. 338–346.

[37] Kaneti, Y. V., S. Tanaka, Y. Jikihara, T. Nakayama, Y. Bando, M. Haruta, et al. Room temperature carbon monoxide oxidation based on two-dimensional gold-loaded mesoporous iron oxide nanoflakes. *Chemical Communications (Cambridge)*, Vol. 54, No. 61, 2018, pp. 8514–8517.

[38] Karimi, A., E. Fatehifar, and R. Alizadeh. Synthesis and Characterization of Nanostructured CuO/CeO_2 Catalysts via Ultrasound Assisted Techniques used for Selective Oxidation of CO. Iranian Journal of Chemical Engineering, Vol. 10, 2013, pp. 51–59.

[39] Guoxing, C., L. I. Qiaoling, W. E. I. Yucai, F. Weiping, and Y. Yiquan. Low-temperature CO oxidation on Ni-promoted $CuO\text{-}CeO_2$ catalysts. Chinese Journal of Catalysis, Vol. 34, 2013, pp. 322–329.

[40] Sun, S., D. Mao, J. Yu, Z. Yang, G. Lu, and Z. Ma. Low-temperature CO oxidation on CuO/CeO_2 catalysts: The significant effect of copper precursor and calcination temperature. *Catalysis Science & Technology*, Vol. 5, No. 6, 2015, pp. 3166–3181.

[41] Wang, L., G. Yin, Y. Yang, and X. Zhang. Enhanced CO oxidation and toluene oxidation on CuCeZr catalysts derived from UiO-66 metal organic frameworks. *Reaction Kinetics, Mechanisms and Catalysis*, Vol. 128, No. 1, 2019, pp. 193–204.

[42] Y.Wang, Y. Yang, N. Liu, Y.Wang, and X. Zhang. Sword-like CuO/CeO_2 composites derived from a Ce-BTC metal-organic framework with superior CO oxidation performance. Royal Society of Chemistry Advances, Vol. 8, No. 58, 2018, pp. 33096-33102.

[43] Zhang, X., X. Zhang, L. Song, F. Hou, Y. Yang, Y. Wang, and N. Liu. Enhanced catalytic performance for CO oxidation and preferential CO oxidation over CuO/CeO_2 catalysts synthesized from metal organic framework: Effects of preparation methods. *International Journal of Hydrogen Energy*, Vol. 43, No. 39, 2018, pp. 18279–18288.

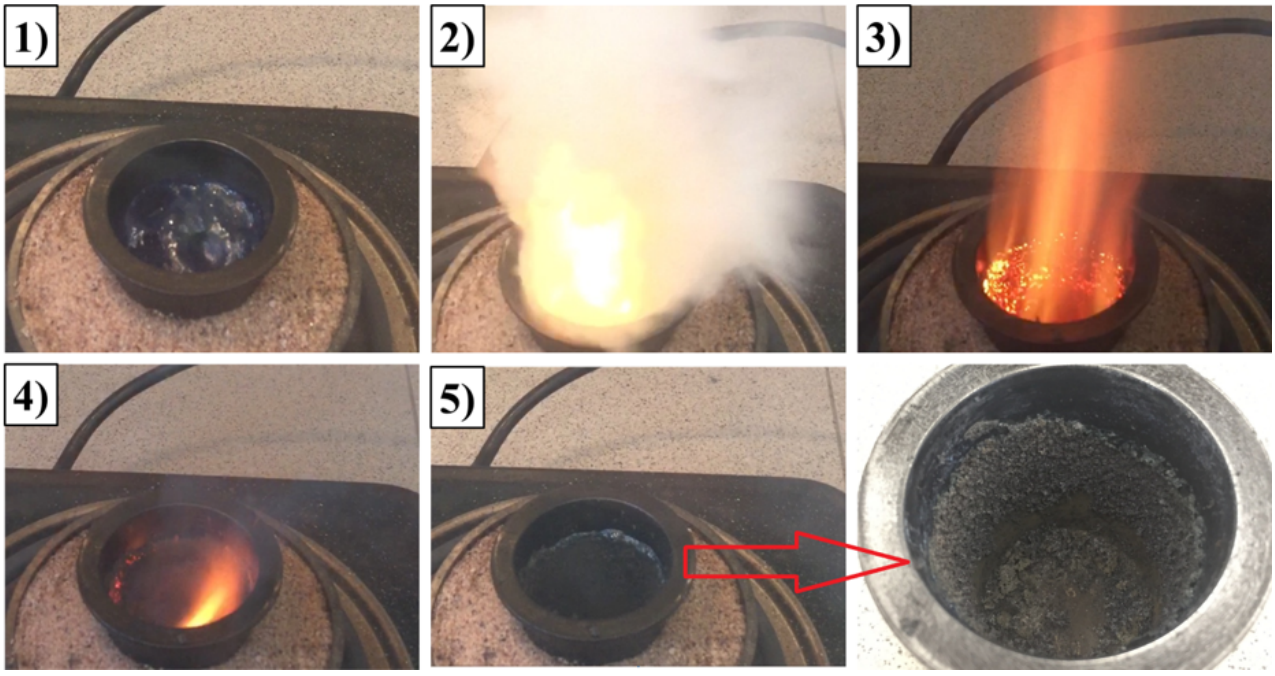

Appendix 1: Synthesis of CuO/CeO_2 composite in solution combustion method (SCS) used urea as the fuel can be divided into stages: after preheating where free and a portion of the water evaporates the reaction mixture foams (1), then at some temperature, it ignites (2), burns (3) and follows by the cooling stage (4) to form an as-synthesized powder.

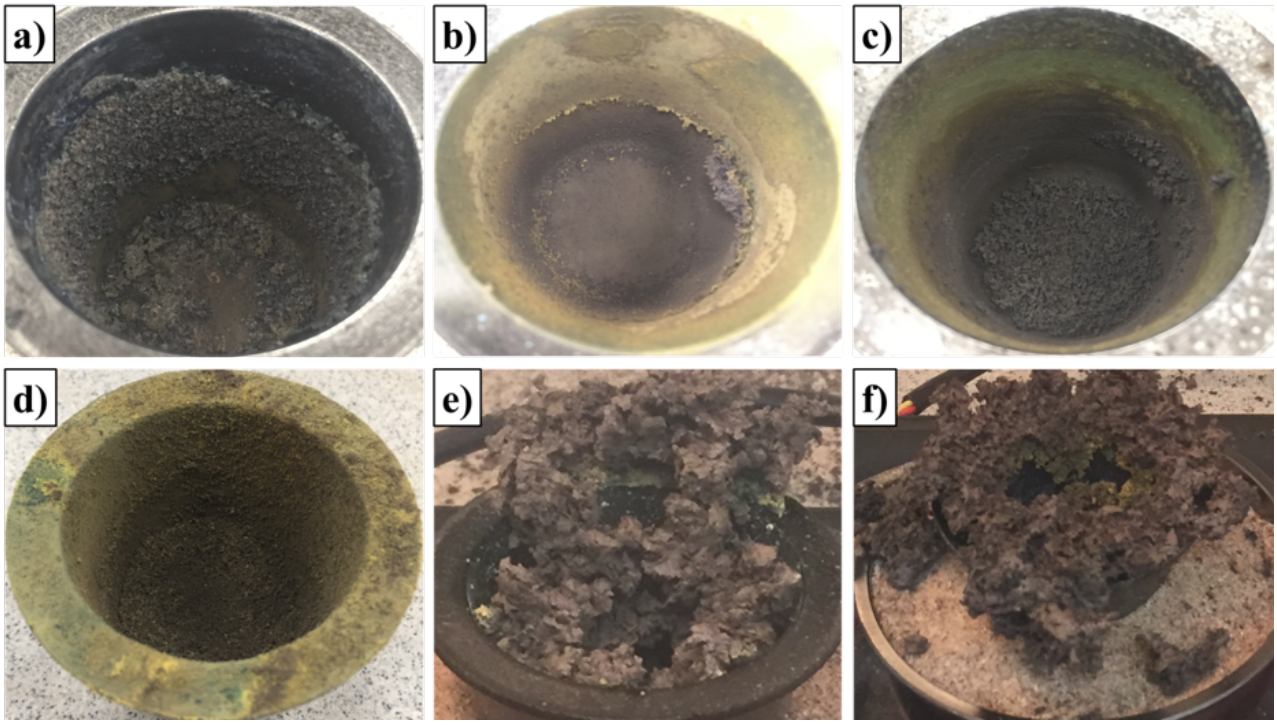

Appendix 2: The as-synthesized powders of CuO/CeO_2 catalysts derived from SCS method using different fuels: a) CuO/CeO_2-urea; b) CuO/CeO_2-glycine; c) CuO/CeO_2-urotropine; d) CuO/CeO_2-ascorbic; e) CuO/CeO_2-citric; f) CuO/CeO_2-glucose.

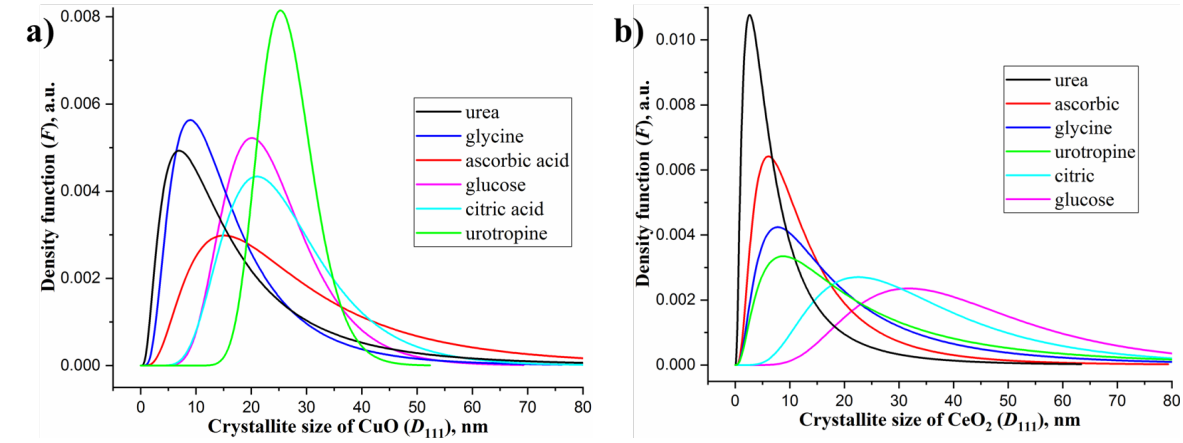

(a) (b)

Appendix 3: Crystallite size distribution of copper(II) oxide and cerium(IV) oxide in CuO/CeO_2 samples of the (111) diffraction peak.